Supporting information for

# Electronic Structure and Photoelectrochemical Properties of an Ir-Doped $SrTiO_3$ Photocatalyst

*Seiji Kawasaki,*[*,†] *Ryota Takahashi,*[†] *Kazuto Akagi,*[‡] *Jun Yoshinobu,*[†] *Fumio Komori,*[†]

*Koji Horiba,*[§] *Hiroshi Kumigashira,*[§] *Katsuya Iwashina,*[¶] *Akihiko Kudo,*[¶] *Mikk Lippmaa*[*,†]

† Institute for Solid State Physics, University of Tokyo, Chiba 277-8581, Japan

‡ WPI-Advanced Institute for Materials Research (WPI-AIMR), Tohoku University, Sendai 980-8577, Japan

§ Photon Factory, High Energy Accelerator Research Organization, Tsukuba 305-0801, Japan

¶ Faculty of Science, Tokyo University of Science, Tokyo 162-8601, Japan

**Corresponding Author**

* E-mail: skawasaki@sci-res.net., * E-mail: mlippmaa@issp.u-tokyo.ac.jp.

Tel: +81-4-7136-3315, Fax: +81-4-7136-3319

## Materials and methods

Figure S1 shows the X-ray diffraction (XRD) patterns of Ir(x at %):$SrTiO_3$ (x = 1, 3, 5) powders used in this study, together with reference data for $IrO_2$, $Sr_3Ti_2O_7$, and $SrTiO_3$. The XRD patterns of the powder samples match the $SrTiO_3$ reference but may also contain a small amount of the layered perovskite $Sr_3Ti_2O_7$. No diffraction peaks of $IrO_2$ were observed. These powders were processed to pellet shapes for use as targets in pulsed laser deposition (PLD) growth of epitaxial thin films.

Typical XRD patterns of Ir(5 at %):$SrTiO_3$ thin film samples deposited on $SrTiO_3$ (001) substrates are shown in Figure S2. The samples were deposited at 700 °C under oxygen pressures of $10^{-1}$ or $10^{-6}$ Torr, producing $Ir^{4+}$ and $Ir^{3+}$ doped $SrTiO_3$ films, respectively. All films were epitaxially grown on $SrTiO_3$ (001) substrates. The slight shift of the XRD peaks of the film grown at $10^{-6}$ Torr is caused by the presence of oxygen defects that occur due to the low growth pressure[1] and also due to the difference of ionic radii of $Ir^{3+}$(0.68 Å) and

$Ir^{4+}$(0.625 Å).[2] The presence of oxygen vacancies stabilizes the $Ir^{3+}$ dopant state at the $Ti^{4+}$ lattice site in $SrTiO_3$ by maintaining charge neutrality.

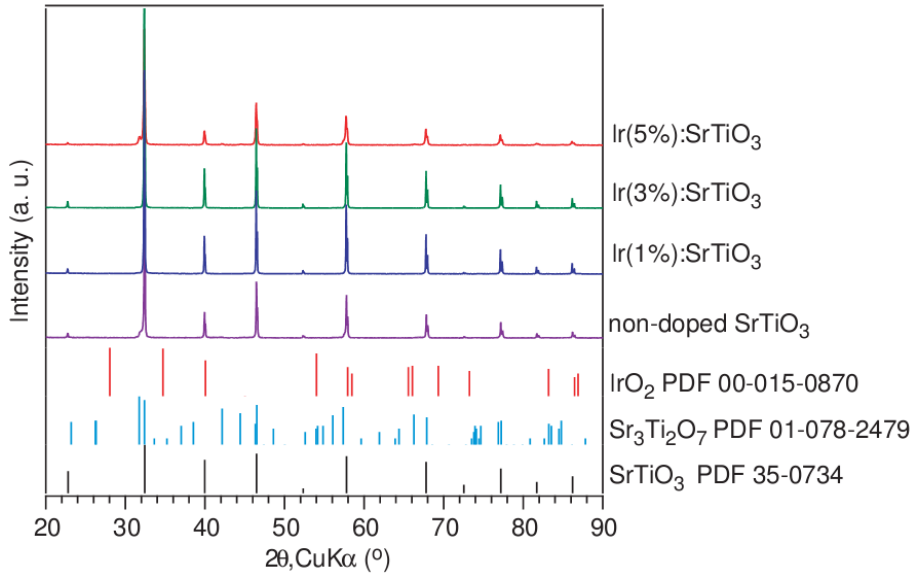


**Figure S1.** XRD patterns of Ir:$SrTiO_3$ powder samples. From top to bottom, data for $Ir^{4+}$(5, 3, 1%):$SrTiO_3$ and non-doped $SrTiO_3$ are shown together with reference data for $IrO_2$, $Sr_3Ti_2O_7$, and $SrTiO_3$.

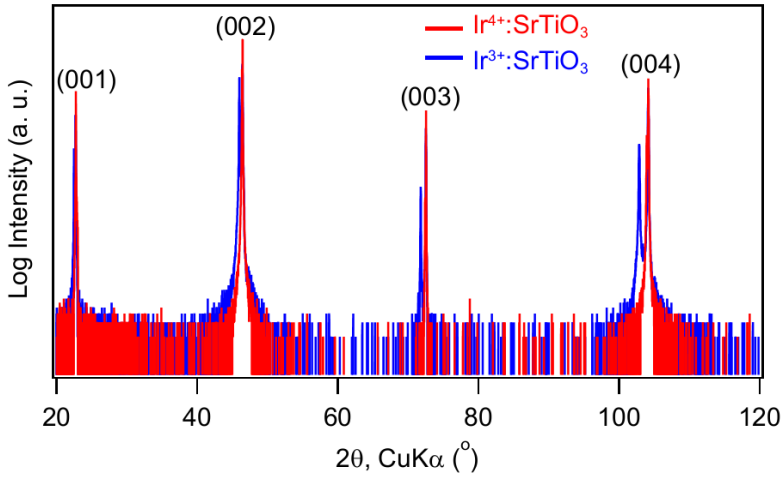


**Figure S2.** XRD patterns of Ir(5 at %):$SrTiO_3$ thin film samples grown on $SrTiO_3$ (001) substrates. The samples were deposited at 700 °C and an oxygen pressure of $10^{-1}$ (red) and $10^{-6}$ Torr (blue).

**X-ray photoelectron spectroscopy (XPS)**

High resolution X-ray photoelectron spectroscopy was performed using the synchrotron light source at BL2 of the Photon Factory (Tsukuba, Japan). Figure S3 shows the atomic subshell photoionization cross sections of Ir 5d, O 2p, and Ti 3d electrons as a function of the incident photon energy, calculated from literature values.[3] The Ir 5d / O 2p and Ir 5d / Ti 3d spectral ratios increase monotonically with the increase of the photon energy from 200 to 1600 eV. Therefore, element-selective photoelectron spectra for Ir 5d can be obtained by changing the photon energy from 600 to 1400 eV and looking for spectral features that increase in intensity at higher photon energies (Figure 5 in the main text).

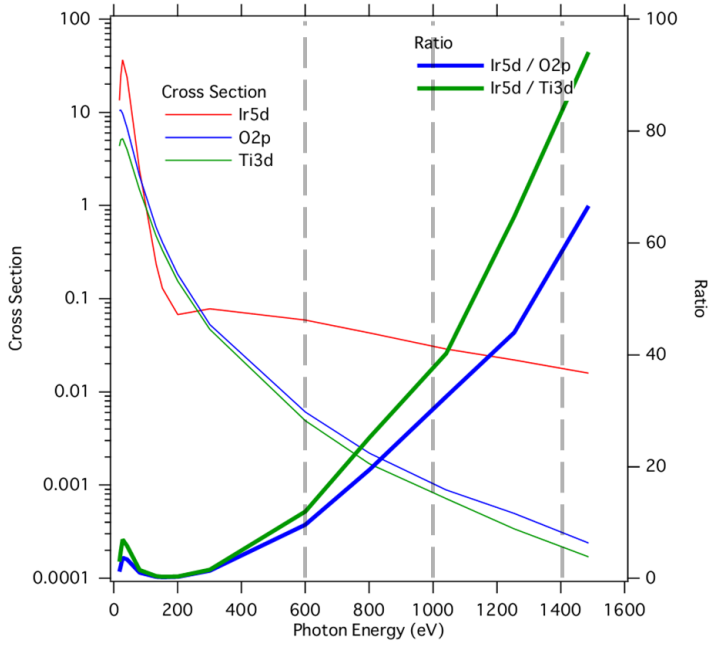


**Figure S3.** Atomic subshell photoionization cross sections for Ir 5d, O 2p, and Ti 3d electrons as a function of the incident X-ray photon energy.

Radiation damage was clearly observed when films were irradiated by the synchrotron light at hν = 600 eV in ultrahigh vacuum (~5 × $10^{-10}$ Torr). Figure S4 shows the first and 10th scans of the Ir 4f core level photoelectron spectra for a film sample deposited at 700 °C and $10^{-1}$ Torr. The Ir 4f core-level spectrum is a doublet consisting of Ir $4f_{7/2}$ and Ir $4f_{5/2}$ components. Ten scans were measured in a sequence after selecting a fresh point on the film surface. The measurement time for a single scan was 1.5 min. It is clear that the $Ir^{4+}$ is easily reduced to $Ir^{3+}$ under strong X-ray irradiation probably due to the photodesorption of

oxygen from the crystal lattice. Therefore, the film composition was analyzed by measuring Ir 4f core level spectra with a laboratory Mg Kα x-ray source (JEOL; JPS-9010MC, hν = 1253.6 eV) instead of a synchrotron light source.

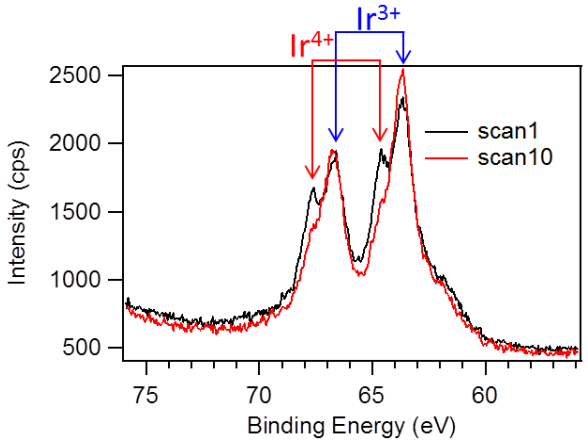


**Figure S4.** The first and the 10th scan of the Ir 4f core level photoelectron spectra for a film sample deposited at 700 °C and $10^{-1}$ Torr. The scans were taken continuously at the same sample position, with each scan lasting 1.5 min. The photon energy was 600 eV.

The Fermi level position of doped $SrTiO_3$ can be inferred from the valence band spectral feature shifts in XPS spectra. Figure S5 shows synchrotron X-ray photoelectron spectra of the valence band of Ir(5%):$SrTiO_3$ films deposited at 700 °C, $10^{-1}$ Torr and 700 °C, $10^{-6}$ Torr, an oxygen-deficient Rh(5%):$SrTiO_3$ film deposited at 700 °C, $10^{-1}$ Torr and annealed at 600 °C, $10^{-6}$ Torr for 2 hours, and a Nb(0.05wt%):$SrTiO_3$ substrate. The spectral intensity differences among the samples are caused by cross section differences that depend on the incident photon energy, but these differences can be ignored when discussing the energy level positions of the O2p-π and O2p-σ components. In this case, the Rh:$SrTiO_3$ sample was intentionally reduced and contained both $Rh^{3+}$ and $Rh^{4+}$ ($Rh^{3+}/Rh^{4+}\approx1$) features. It showed a −0.5 eV shift of the VB from the other spectra, indicating that the Fermi level of Rh:$SrTiO_3$ is 0.5 eV deeper than that of Nb:$SrTiO_3$, which leads to the p-typeness observed in this material. However, the binding energy positions of O2p-π and O2p-σ of Ir:$SrTiO_3$ were at the same positions of those of Nb:$SrTiO_3$, regardless of the Ir valence, showing that the Fermi level positions of Ir:$SrTiO_3$ and Nb:$SrTiO_3$ are similar, although the first-principles calculations predicted that the Fermi level of Ir:$SrTiO_3$ should be deeper than that of non-doped $SrTiO_3$ (Figure 4). One possible reason for the difference between the results

obtained from XPS and simulations might be related to oxygen defect formation in the samples, especially in the surface layer of the films.

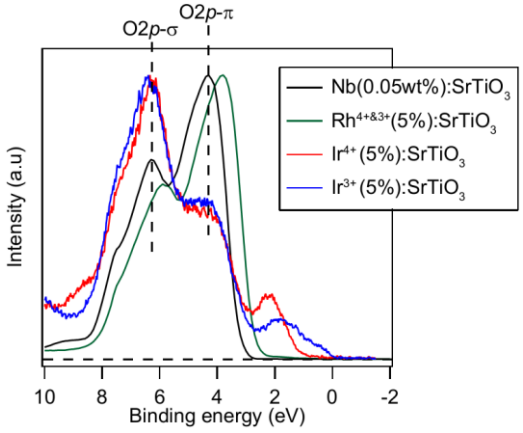


**Figure S5.** Synchrotron X-ray photoelectron spectra of the valence band of Ir(5%):$SrTiO_3$ films deposited at 700 °C, $10^{-1}$ Torr (red) and 700 °C, $10^{-6}$ Torr (blue), Rh(5%):$SrTiO_3$ film deposited at 700 °C,$10^{-1}$Torr and annealed at 600 °C, $10^{-6}$ Torr for 2 hours (green), and Nb(0.05wt%):$SrTiO_3$ substrate. The photon energy was set at 1000 eV for $Ir^{4+/3+}$:$SrTiO_3$ and 160 eV for Rh:$SrTiO_3$ and Nb:$SrTiO_3$ samples. The binding energy was referenced to the Au Fermi level position at 0 eV.

**Density of states calculations**

A 3 × 3 × 3 cell was used in the calculations. One of the Ti atoms was substituted by $Ir^{4+}$ to calculate the density of states (DOS) of an isovalent sample. While the GGA/PBE96[4] functional underestimated the band-gap width (ca. 1.5 eV for $SrTiO_3$) and failed to describe the in-gap states, the hybrid functional HSE06 accurately reproduced the band-gap width (ca. 3.0 eV for $SrTiO_3$) and successfully described both the valence band and mid-gap states (Figures S6 and S7). The HSE06 functional was therefore used for all calculations presented in this paper.

The PAW method[5, 6] was used for effective atomic potentials with the cutoff energy of the plane wave basis set at 400 eV. After a comparison of 2 × 2 × 2 and 4 × 4 × 4 Monkhorst-Pack k-point meshes,[7] the 2 × 2 × 2 mesh was adopted. Gaussian smearing was applied with a width of 0.2 eV. The lattice constant was set to the experimental value of 3.905 Å. Structure optimization was done using the HSE06 functional until the maximum force became less than 0.03 eV/Å. While the $Ti^{4+}$-O distance in a $SrTiO_3$ crystal was 1.95Å, $Ir^{4+}$-O and $Ir^{3+}$-O distances were 1.98Å and 2.01Å, respectively. The DOS data were

calculated based on these optimized structures. The $Ir^{3+}$:$SrTiO_3$ system was modeled by injecting an excess electron with the same amount of uniform background counter charge. Molecular energy level diagrams for the $Ir^{4+}$ and $Ir^{3+}$ dopants are shown in Figure S8.

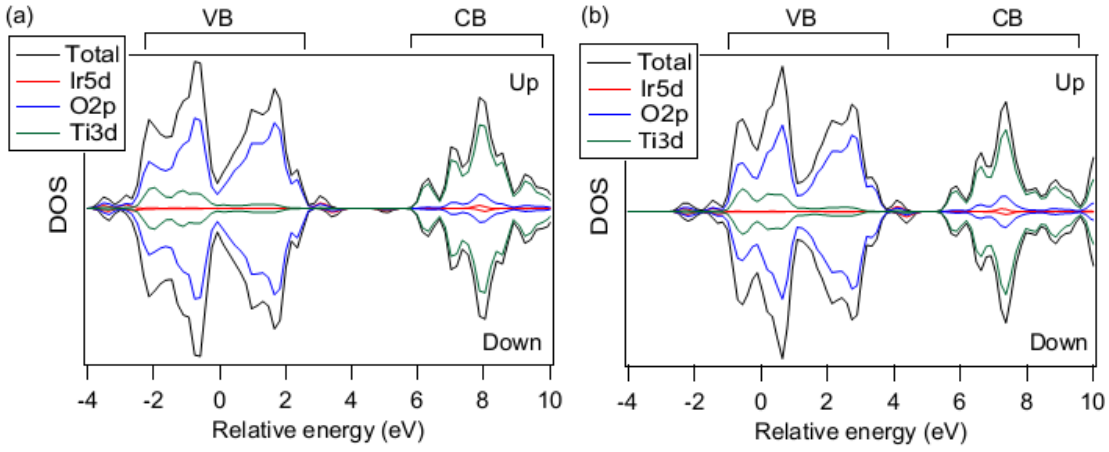


**Figure S6.** Total DOS (black) and PDOS of Ir 5d (red), O 2p (blue), and Ti 3d (green) for $Ir^{4+}$:(3.7 at%):$SrTiO_3$ obtained by first-principles calculations using (a) the HSE06 functional and (b) the GGA/PBE96 functional. Up and down spin states are shown in the upper and lower parts of the figures, respectively. Up and down spin states are distinguished in this system due to the existence of an unpaired electron at the $Ir^{4+}$ site.

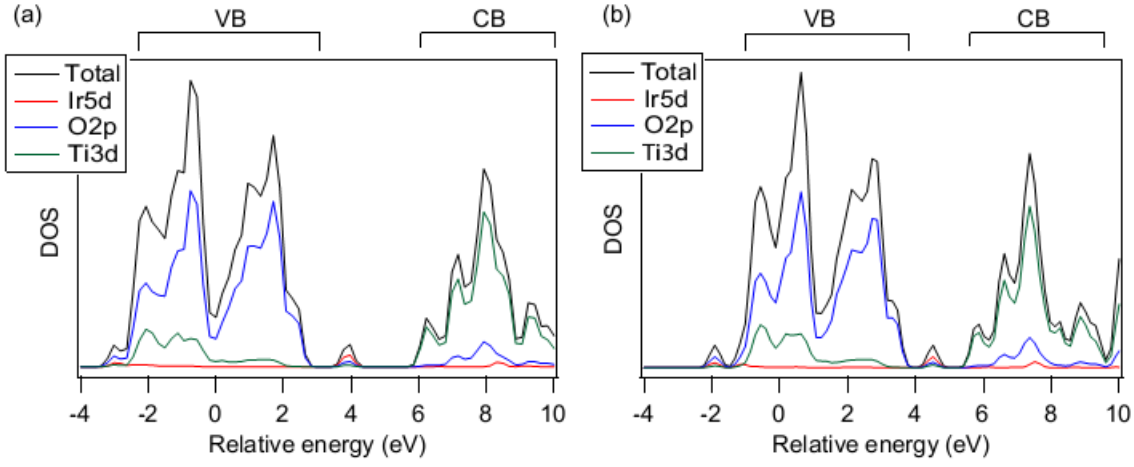


**Figure S7.** Total DOS (black) and PDOS of Ir 5d (red), O 2p (blue), and Ti 3d (green) for $Ir^{3+}$:(3.7 at%):$SrTiO_3$ obtained by first-principles calculations using (a) the HSE06 functional

and (b) the GGA/PBE96 functional. Up and down spin states are not distinguished in this system, since both up and down spin states are located at the same energy positions due to the absence of any magnetic anisotropy in this system.

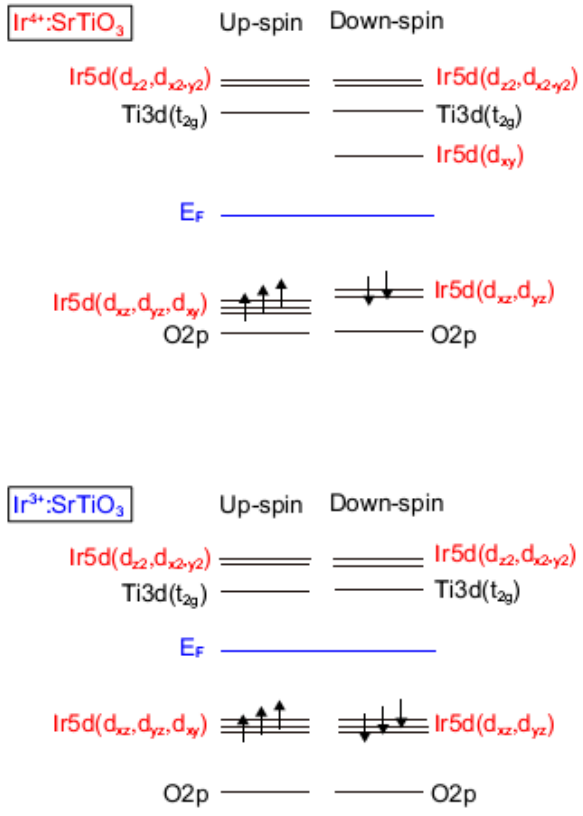


**Figure S8.** Molecular energy diagram for the $Ir^{4+}$ and $Ir^{3+}$ sites.


(1) Ohnishi, T.; Lippmaa, M.; Yamamoto, T.; Meguro, S.; Koinuma, H. Improved Stoichiometry and Misfit Control in Perovskite Thin Film Formation at a Critical Fluence by Pulsed Laser Deposition. *Appl. Phys. Lett.* **2005**, *87*, 241919.

(2) Shannon, R. D. Revised Effective Ionic Radii and Systematic Studies of Interatomic Distances in Halides and Chalcogenides. *Acta Cryst. A* **1976**, *32*, 751-767.

(3) Yeh, J. J.; Lindau, I. Atomic Subshell Photoionization Cross Sections and Asymmetry Parameters: 1≤Z≤103. *At. Data Nucl. Data Tables* **1985**, *32*, 1-155.

(4) Perdew, J. P.; Burke, K.; Ernzerhof, M. Generalized Gradient Approximation Made Simple. *Phys. Rev. Lett.* **1996**, *77*, 3865-3868.

(5) Blöchl, P. E. Projector Augmented-Wave Method. *Phys. Rev. B* **1994**, *50*, 17953-17979.
(6) Kresse G.; Joubert. D. From Ultrasoft Pseudopotentials to the Projector Augmented-Wave Method. *Phys. Rev. B* **1999**, *59*, 1758-1775.
(7) Monkhorst, H. J.; Pack, J. D. Special Points for Brillouin-Zone Integrations. *Phys. Rev. B* **1976**, *13*, 5188-5192.